nature astronomy

ARTICLES

https://doi.org/10.1038/s41550-019-0737-8

A cometary building block in a primitive asteroidal meteorite

Larry R. Nittler[1]*, Rhonda M. Stroud[2], Josep M. Trigo-Rodríguez[3,4], Bradley T. De Gregorio[2], Conel M. O'D. Alexander[1], Jemma Davidson[1,5], Carles E. Moyano-Cambero[3,4] and Safoura Tanbakouei[3,4]

Meteorites originating from primitive C-type asteroids are composed of materials from the Sun's protoplanetary disk, including up to a few per cent organic carbon. In contrast, some interplanetary dust particles and micrometeorites have much higher carbon contents, up to >90%, and are thought to originate from icy outer Solar System bodies and comets. Here we report an approximately 100-μm-diameter very carbon-rich clast, with highly primitive characteristics, in the matrix of a CR2 chondrite, LaPaz Icefield 02342. The clast may represent a cometary building block, largely unsampled in meteorite collections, that was captured by a C-type asteroid during the early stages of planet formation. The existence of this cometary microxenolith supports the idea of a radially inward transport of materials from the outer protoplanetary disk into the CR chondrite reservoir during the formation of planetesimals. Moreover, the H-isotopic composition of the clast is suggestive of a temporal evolution of organic isotopic compositions in the comet-forming region of the disk.

Carbonaceous chondrite meteorites may have formed beyond the original orbit of Jupiter[1]. The Renazzo-like (CR) chondrites are among the most primitive (that is, least modified) meteorites[2], on the basis of their abundant presolar grains, diversity of complex organic compounds and bulk isotopic anomalies in elements such as Cr and Mg[3–5]. The aqueous alteration histories of the CR chondrites in their asteroidal parent body varies widely[6], ranging from extensively altered to nearly pristine. Although the matrices of the most primitive carbonaceous chondrites, including the least altered CRs, bear some chemical and mineralogical similarities to anhydrous chondritic-porous interplanetary dust particles (CP-IDPs) that are thought to originate from comets, in general they have lower bulk C contents. Whereas CR chondrites typically have 1.0–1.4 wt% C in bulk, and roughly three times that in their matrices, CP-IDPs, which range in size up to tens of micrometres, have on average approximately 15 wt% C[7,8]. An additional class of astromaterials known as ultracarbonaceous Antarctic micrometeorites (UCAMMs), range up to several hundred micrometres in diameter and contain up to >90 wt% C[9–11]. Comets and/or other primitive outer Solar System bodies have been suggested to be the sources of both IDPs and UCAMMs.

The Antarctic CR2 chondrite LaPaz Icefield (LAP) 02342 is one of the least terrestrially weathered CR chondrites and exhibits heterogeneity in its degree of aqueous alteration on submillimetre scales[12,13]. We report here the detailed characterization of an unusual C-rich clast (CRC) in this meteorite. The CRC is a xenolith, likely a cometary building block captured by a C-type asteroid during its accretion, and thus provides information about radial transport of materials in the outer protoplanetary disk during the formation of planetesimals. Moreover, the mineralogical and chemical composition of this clast may be characteristic of cometary materials that are not represented in meteorite collections because they are too fragile to survive atmospheric entry[14].

Carbon-rich clast

Scanning electron microscopy (SEM) of a LAP 02342 section revealed an approximately 100-μm-diameter CRC embedded in fine-grained matrix adjacent to a chondrule (Fig. 1 and Methods). The CRC is dominated by a fine-grained carbonaceous material, intermixed with inorganic materials. As seen in SEM-based energy dispersive X-ray spectroscopy (EDS) maps, it is enriched in Na, relative to the surrounding matrix, and S correlates with Na within the clast. We mapped the clast, as well as the nearby matrix (Fig. 1b) and a highly altered S-rich chondrule rim (Supplementary Fig. 1) by nanoscale secondary ion mass spectrometry (NanoSIMS) for H, C, N and O abundances and isotopes. This was followed by focused-ion-beam (FIB) lift-out of ultrathin sections from both the CRC and matrix (see Methods). The extracted sections were analysed by aberration-corrected scanning transmission electron microscopy (STEM), and synchrotron-based X-ray absorption near-edge spectroscopy (XANES).

Isotopic characteristics

NanoSIMS O isotope mapping of the LAP 02342 section identified 18 grains with highly non-solar O isotope ratios indicating that they are presolar circumstellar grains (Fig. 2a and Supplementary Table 1). Their isotopic ratios are within the range of previous studies of presolar O-rich grains[15] and indicate an origin in asymptotic giant branch stars (a late evolutionary stage of stars of mass up to a few times that of the Sun). The NanoSIMS $^{28}Si^-/^{16}O^-$ and $^{27}Al^{16}O^-/^{16}O^-$ ion ratios of the grains are consistent with them being most likely silicates[16] and not Al-rich oxides.

Five presolar O-rich grains each were found in the CRC and S-rich chondrule rim, with the remaining eight found in the matrix. However, the measured area of the CRC made up only approximately 12% of the total imaged area, suggesting a higher abundance

---

[1]Department of Terrestrial Magnetism, Carnegie Institution of Washington, Washington, DC, USA. [2]Materials Science and Technology Division, Code 6366, US Naval Research Laboratory, Washington, DC, USA. [3]Meteorites, Minor Bodies and Planetary Sciences Group, Institute of Space Sciences (CSIC), Barcelona, Catalonia, Spain. [4]Institut d'Estudis Espacials de Catalunya (IEEC), Barcelona, Catalonia, Spain. [5]Center for Meteorite Studies, School of Earth and Space Exploration, Arizona State University, Tempe, AZ, USA. *e-mail: lnittler@ciw.edu

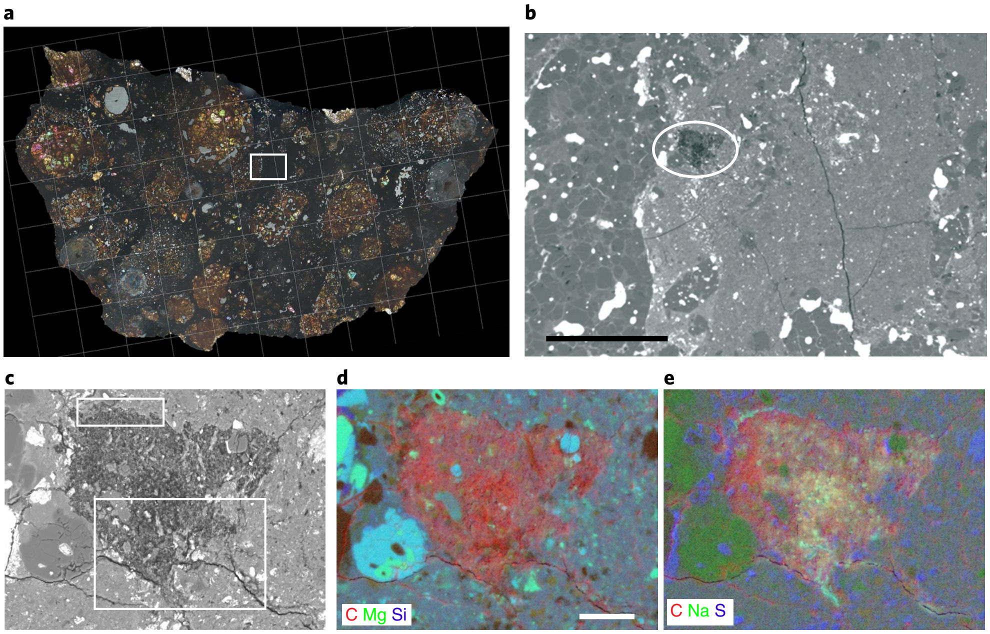

Fig. 1 | CRC in section of LAP 02342 meteorite. a, The polished thin section in transmitted polarized light. The box indicates location of **b**. **b**, SEM micrograph of the CRC and nearby matrix. Scale bar, 250 μm. **c**, SEM of CRC. **d**,**e**, RGB composite of EDS elemental maps of the CRC. Scale bar, 25 μm. The clast is approximately 70 area% C and is relatively enriched in both Na and S. Boxes in **c** correspond to regions shown in Figs. 3 and 4.

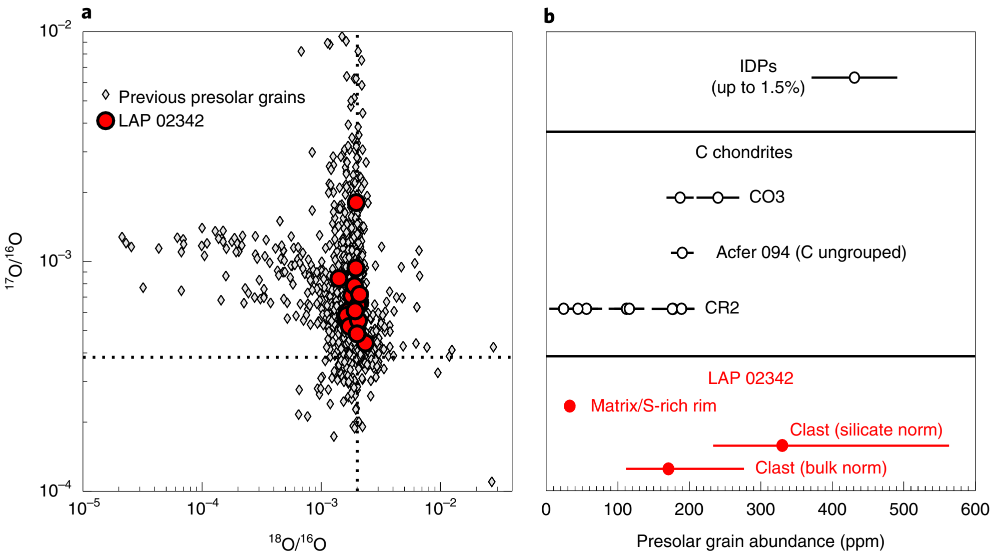

Fig. 2 | O-rich presolar grains in LAP 02342. a, Oxygen three-isotope plot of presolar O-rich grains in LAP 02342 (red circles) compared with those previously reported in meteorites and IDPs. **b**, Abundances of presolar O-rich grains in LAP 02342 compared with those in IDPs and carbonaceous chondrites. See ref. [15] for data sources. The circles and horizontal error bars indicate the average abundance and 1σ error for IDPs, average abundances and 1σ errors for individual C chondrites, and average abundances and 1σ errors for different regions of LAP 02342.

of presolar grains in the CRC than in the meteorite's matrix. We calculated the concentrations of presolar grains in the different imaged regions by dividing the total area occupied by the grains by the total imaged area for each region (Methods). The total abundance of presolar O-rich grains in the LAP 02342 matrix and S-rich rim was found to be 30^{+11}_{-7} ppm (1σ), in the range of other CR2 chondrites (Fig. 2b). This abundance is lower than in the most primitive chondrites (for example, Acfer 094, CO3 chondrites) and CP-IDPs, due to destruction by parent-body aqueous alteration. In contrast, the presolar grain abundance is much higher in the CRC, 360^{+200}_{-130} ppm (1σ). This value is calculated from the total amount of the imaged area of the clast that is O rich for direct comparison with other silicate-dominated materials. If the total area of the clast, including the dominant C-rich material, is considered, and the organic matter is assumed to have a density half that of silicates, the estimated abundance would fall to 175^{+100}_{-65} ppm. The uncertainty is large due to there being only five grains, but the abundance is certainly higher than that in the host meteorite and comparable to the highest abundances observed in meteorite matrices and, notably, to many CP-IDPs. Eight ^{13}C-rich presolar SiC grains were identified as

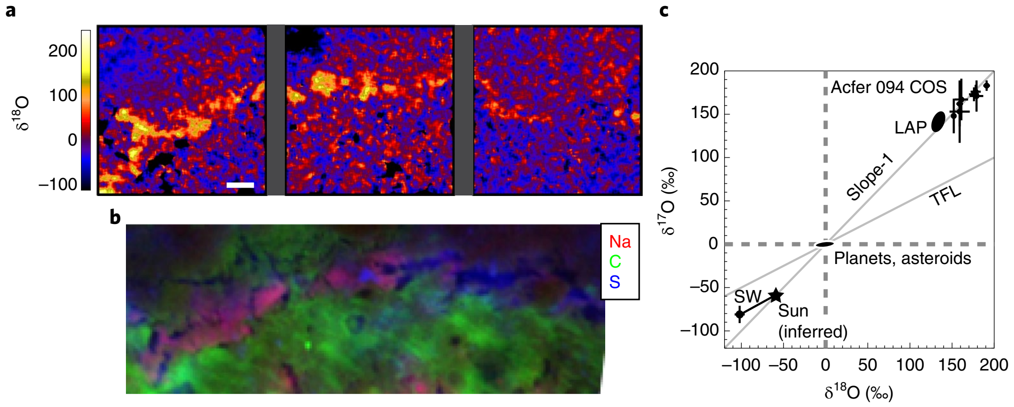

Fig. 3 | ^{16}O-poor material in the CRC. a, $\delta^{18}O$ images showing anomalous ^{16}O-poor grains near the upper border of the CRC (upper box in Fig. 1c); additional ^{16}O-poor grains were found in the clast interior. Scale bar, 2 μm. **b**, SEM-EDS composite colour map. Red, sodium; green, carbon; blue, sulfur. The O anomalous materials are rich in Na and S, and were revealed by STEM data to be Na-rich sulfates. **c**, Oxygen three-isotope plot of the Solar System. The ^{16}O-poor materials in the LAP 02342 CRC are represented by a $2\sigma_{\text{mean}}$ error ellipse calculated from the 42 most anomalous grains (Supplementary Table 2) identified in the NanoSIMS images. Delta values are per mil variations of an isotopic ratio R from a standard ratio R_{std}: $\delta R = 1{,}000 \times (R/R_{\text{std}} - 1)$. Here, R_{std} values correspond to those of standard mean ocean water (dashed lines). Data for Acfer 094 COS[20] and the Sun (inferred from the solar wind (SW) composition)[38] are shown for comparison. TFL is the terrestrial mass fractionation line, and the line of slope 1 connecting the Sun to planetary compositions is also shown.

well within the matrix and S-rich rim, indicating a SiC abundance of approximately 30 ppm, which is consistent with that seen in many chondrite groups[17].

In addition to presolar grains, the NanoSIMS measurements also identified some micrometre-sized materials in the CRC with unusual O isotopic compositions of $\delta^{17}O \approx \delta^{18}O \approx 100$–200‰ (Fig. 3). These grains were most obviously present near the outer edge of the clast, though several were found in the interior. SEM-EDS mapping and STEM observations (below) indicate that they are Na-rich sulfate minerals. The ^{16}O-poor signature is reminiscent of the 'cosmic symplectite' (COS) found in the ungrouped Acfer 094 carbonaceous chondrite[18] as well as isotopically similar, but mineralogically different, materials in IDPs[19]. Acfer 094 COS is a fine-grained aggregate of magnetite and iron sulfide, and its O isotopic composition is believed to reflect a ^{16}O-poor water reservoir that was present in the solar nebula. Based on the imaged area (see Methods), we estimate a lower limit on the abundance of O anomalous material in the CRC of 0.3 wt%.

H, C and N isotope mapping revealed that the LAP 02342 matrix and S-rich rim contain ubiquitous macromolecular organic inclusions (0.1–1.0 μm across) that are variably enriched in D and ^{15}N, similar to that seen in other CR chondrites[20]. The organic matter (OM) within the CRC is also isotopically anomalous but less so than that in the host meteorite (Fig. 4 and Supplementary Fig. 2). Whereas the matrix OM grains have average values of $\delta D \approx 1{,}060$‰ and $\delta^{15}N \approx 200$‰, the CRC has average values of $\delta D \approx 130$‰ and $\delta^{15}N \approx 0$‰. Regions of much more highly enriched D and/or ^{15}N ('hotspots'), ranging up to a few micrometres in size, make up approximately 4 area% of the CRC, compared with some two to three times higher abundance of hotspots in the matrix and S-rich rim (Supplementary Fig. 2). The H/C and N/C ratios could not be quantified for the OM, but are comparable to or slightly lower in the CRC compared with the matrix OM (for reference, typical CR chondrite insoluble OM[3] has $H/C \approx 0.75$ and $N/C \approx 0.035$).

Organic chemistry

XANES at the C K-edge revealed that the OM within the CRC differs from that of the surrounding matrix. C-XANES spectra (Fig. 4) of OM in FIB sections extracted from both the CRC (edge and interior) and matrix show absorption peaks that are attributable to aromatic C (285.0 eV), ketone functional groups (286.5 eV) and carboxyl functional groups (288.2 eV), which is typical of primitive chondritic insoluble OM[21,22]. However, the abundances of the O-bearing ketone and carboxyl functional groups in the spectra of the CRC edge and interior sections are progressively lower, relative to the aromatic C peak, than in spectra from matrix OM. Assuming that the relative abundances of major organic functional groups were modified by interaction with hydrothermal fluids in the parent asteroid[23], these data suggest that these parent-body fluids were not able to effectively penetrate and alter the organic functional chemistry of the CRC, consistent with the high presolar silicate abundance. As observed by SIMS and STEM-EDS, the N abundance of the CRC OM is low ($N/C < 0.005$), and N-XANES spectra did not contain appreciable absorption peaks.

Mineralogical characteristics

STEM analyses of the matrix sections (for example, Fig. 5a and Supplementary Fig. 3) show mineralogical and petrologic characteristics consistent with other CR2 meteorites[24,25]. Silicates, glass and sulfides are abundant. The degree of aqueous alteration is variable, but mostly mild, with some carbonates, but no sulfates and phyllosilicates, present in the matrix sections. Consistent with the NanoSIMS imaging of the surface, the cross-section STEM imaging shows that OM is present as discrete submicrometre- to micrometre-sized blebs. Very little void space is visible, and thus the overall porosity is low.

The CRC sections (for example, Fig. 5b) show larger veins of OM extending several micrometres, and substantial porosity (containing a multitude of approximately 200 nm and larger voids). The OM encloses individual silicate and sulfide grains (Fig. 6 and Supplementary Figs. 3 and 4). Many of the enclosed silicates are chemically and texturally very similar to GEMS (glass with embedded metal and sulfides) grains (Fig. 6, Supplementary Table 3 and Supplementary Figs. 4–6) that are common to both CP-IDPs[23,26] and UCAMMs[9,27]. Like the CP-IDP and UCAMM GEMS, the CRC GEMS have an amorphous silicate ground mass, with internal metal and sulfide subgrains (Fe:Ni > 10), and are occasionally decorated with external sulfides (with Ni < 20 at%). Exposed GEMS (microtomed or otherwise not encapsulated in C) are highly susceptible to

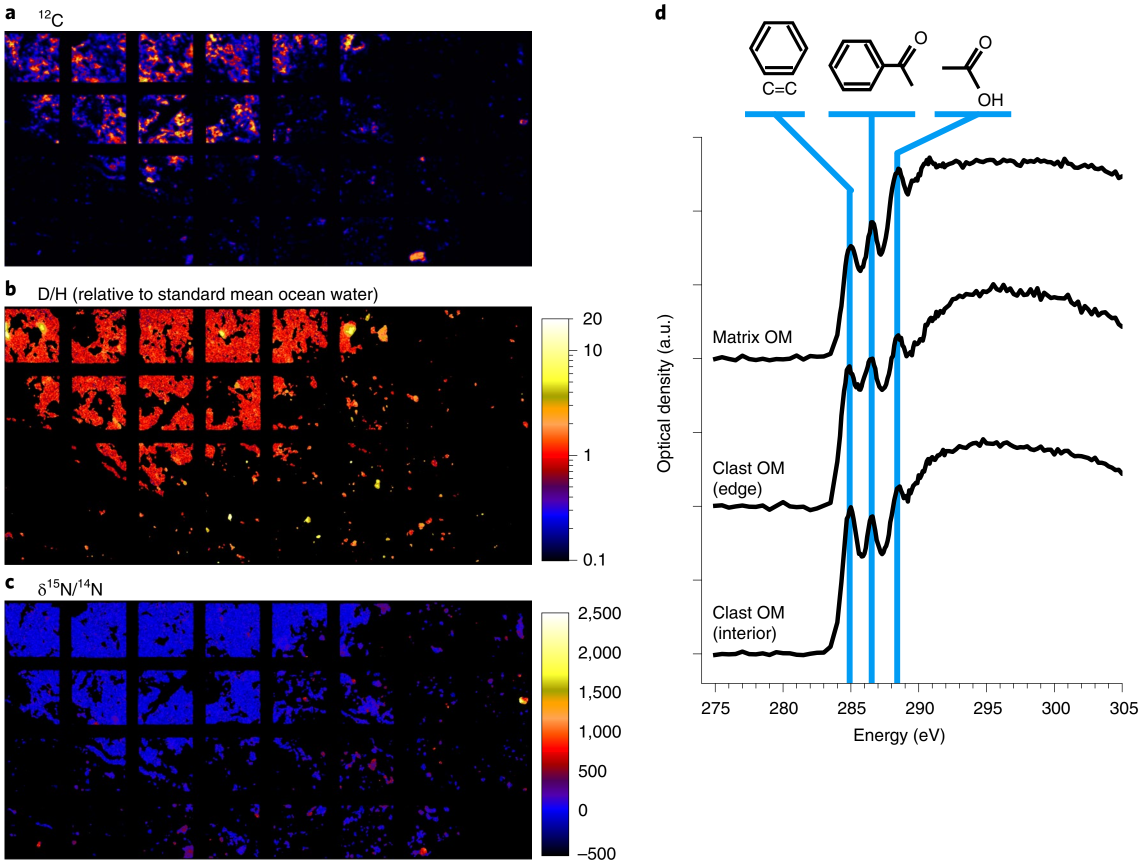

Fig. 4 | OM in CRC. H and N isotopic and functional-group chemistry of organic matter in LAP 02342. **a**–**c**, NanoSIMS image mosaics of ^{12}C (**a**), D/H ratio (logarithmic colour scale), normalized to the terrestrial value of 1.56×10^{-4} (**b**) and δ^{15}N values, normalized to the terrestrial ratio of 0.00367 (**c**), for the CRC and nearby matrix (lower box in Fig. 1c). Compared with the matrix, the CRC is more isotopically homogeneous in H and N, although D and ^{15}N hotspots are present. **d**, C-XANES spectra from OM in FIB sections from the LAP 02342 matrix and the CRC. Vertical blue lines indicate absorptions due to (left to right) aromatic carbon, ketone functional groups and carboxyl functional groups. The section from near the edge of the CRC shows an intermediate functional-group distribution.

aqueous alteration[28] and evidence for aqueously altered GEMS has been reported in one UCAMM[27]. Unlike in IDPs and UCAMMs, however, GEMS-like material has only been reported previously for one meteorite, the relatively unaltered Paris CM2 chondrite[29]. In comparison with the highly pristine and anhydrous GEMS typical of most IDPs and UCAMMs, a substantial fraction of the GEMS grains in the CRC show evidence for a minor level of aqueous alteration. For example, one grain near the top of the section shown in Fig. 5b shows evidence for minor recrystallization and the formation of oxidation rims on metal subgrains (Fig. 7, Supplementary Fig. 6 and Supplementary Table 6). This particular section was extracted from the upper edge of the clast (Fig. 3a and Supplementary Fig. 7) and has abundant Na-sulfate at the SIMS-exposed edge coinciding with the ^{16}O-poor material identified by NanoSIMS. Both the OM and the GEMS grains near the ^{16}O-poor material also show enrichment in Na (Fig. 7), most likely due to deposition from a fluid. No Na was found in the interior of better-preserved GEMS grains (for example, Fig. 6 and Supplementary Fig. 4). Additional Na-rich sulfate grains were observed in other FIB sections from the clast interior, although their isotopic compositions are unknown.

Summary of CRC characteristics

Whereas the mineralogical, isotopic and chemical features of the studied matrix and altered chondrule rim in LAP 02342 are similar to those of other CR2 chondrites, the CRC differs substantially in several important respects. (1) The very high abundance of organic C. Carbonaceous material makes up >70 area% of the CRC and assuming that the carbonaceous material has half the density of the silicates, we estimate that C makes up >50 wt% of the CRC, compared with <3–4 wt% typical of CR matrices[30]. The abundance of C in the CRC is comparable to UCAMMs and the most C-rich IDPs. (2) The higher porosity seen in STEM images (Fig. 5 and Supplementary Fig. 3). (3) The higher apparent abundance of presolar silicates (Fig. 2b) that is comparable to or higher than that seen in the most primitive meteorite matrices, and consistent with the higher values seen in CP-IDPs. (4) The presence of GEMS grains (Figs. 5 and 6 and Supplementary Figs. 4–6) that are very similar to those seen in CP-IDPs and UCAMMs, and generally not seen in chondritic meteorites. (5) The overall high abundance of Na, especially the presence of Na-rich sulfate with a highly anomalous ^{16}O-poor isotopic signature. (6) The distinct isotopic and functional-group nature of the CRC OM (Fig. 4), compared with those in the matrix, especially the lower abundances of O-bearing ketone and carboxyl functional groups. The properties of the CRC point to it being a very primitive xenolithic object that was captured along with fine-grained matrix materials during the accretion of the CR parent asteroid.

Origin and implications of the CRC

Overall, the isotopic and chemical properties of the CRC strongly overlap with those previously seen in both primitive IDPs and UCAMMs, commonly argued to have originated in comets or other

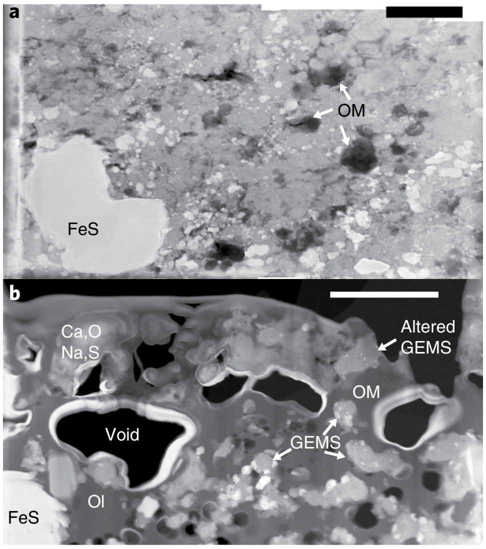

Fig. 5 | FIB sections from LAP 02342. a,**b**, High-angle annular dark-field (HAADF) STEM image mosaics of FIB sections from the matrix (**a**) and the CRC (**b**) of LAP 02342. The matrix contains abundant silicate, glass and sulfides, and rarer discrete nanoscale blebs of organic matter, but minimal porosity. The label OM refers to organic matter, Ol refers to olivine and GEMS is glass with embedded metal and sulfides. Voids (pores) are black. Bright rims at the edges of the larger voids result from redeposition of sputtered material during the FIB preparation. The Na-bearing sulfates and organic matter, determined by SIMS to be ^{16}O poor, are located at the top of the section. Scale bars, 1 µm.

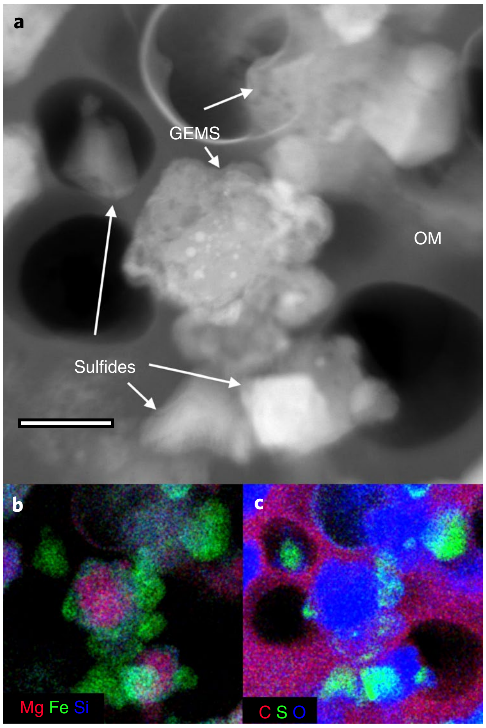

Fig. 6 | STEM data for CRC FIB section. a–**c**, STEM-HAADF (**a**) and EDS colour composite maps corresponding to indicated elements (**b**,**c**) of GEMS and Fe,Ni-sulfides in OM in the CRC in LAP 02342. Metal and sulfide grains internal to the GEMS appear as round, bright features in the HAADF, and can be resolved in the full EDS spectrum images (see Supplementary Fig. 4). Additional quantification of the EDS spectrum images is included in Supplementary Fig. 5 and Supplementary Tables 3, 4 and 5. Scale bar in **a**, 100 nm.

icy outer Solar System bodies. IDPs and UCAMMs have been found to be mineralogically, morphologically, isotopically and chemically diverse[9,10,27,31], suggesting a range of parent bodies, and formation and processing histories. The lower abundance of C=O bonds in the CRC OM (Fig. 4d), relative to matrix OM, is consistent with that seen in UCAMMs, but the CRC does not show the very N-rich compositions seen in some UCAMMs[10,11]. The close-to-terrestrial bulk H and N isotopic compositions of the CRC OM (with some more extreme D and ^{15}N hotspots) differ from some UCAMMs that have extreme isotopic enrichments[9,10], but are quite similar to those of one UCAMM and many IDPs[22,32]. The preservation both of more anomalous OM in the LAP 02342 matrix, and of GEMS and presolar grains in the clast, indicates limited isotopic exchange in the parent body, and thus the lower D/H and ^{15}N/^{14}N of the CRC OM most likely reflects the pre-accretionary composition of the xenolith. We suggest that the CRC formed in the same region of the solar nebula as the materials that accreted to form icy outer Solar System objects and was subsequently mixed into the region where the CR chondrite parent asteroid(s) formed.

The presence of ^{16}O-poor, Na-rich sulfates in the CRC provides an additional link to icy primitive bodies. High Na has been reported for UCAMMs[27] and in fireball emission spectra of bright cometary meteoroids[33,34]. The ^{16}O-poor signature of the sulfate grains is similar to that both of Acfer 094 COS[18] (Fig. 3) and of rare, non-COS, materials in IDPs[19]. This isotopic composition is complementary to the ^{16}O-rich nature of the Sun[35]. It has been argued to represent a water signature in the outer solar nebula that was produced by preferential ultraviolet photodissociation of $C^{17,18}O$ followed by reaction of the liberated O atoms with H to form water. High-precision O isotopic data for cometary ices are not available but are likely to be similarly ^{16}O poor if the CO ultraviolet photodissociation mechanism was responsible for the O isotopic systematics of bulk planetary materials[36,37].

We suggest that before accretion into the LAP 02342 parent body, the CRC consisted of a fine-grained aggregate of OM, inorganic dust and ^{16}O-poor ices. This aggregate may have been in the earliest stages of the nebular accretion process or part of an earlier primitive icy parent body that was subsequently disrupted. Heating led to melting of ices and subsequent formation of sulfate by reaction between water and H_2S or other S-bearing ices in the CRC[38] and minor alteration of some silicates (for example, altered GEMS in Fig. 7). Such heating may have taken place before accretion to the CR asteroidal parent body, for example, during a transient heating event on a prior icy host of the CRC or in the solar nebula, and/or during the heating of the CR parent body itself. The preservation of the ^{16}O-poor isotope signature across the CRC indicates that if the alteration occurred on the CR parent body, there was little exchange of fluids between the CRC and LAP 02342 matrix. Moreover, given that Na is clearly enriched throughout much of the CRC, relative to the matrix (Fig. 1e), the Na in the sulfate likely originated from the CRC itself, but it is unclear in what original chemical form (for example, silicate dust and/or Na-rich OM as seen in at least one UCAMM[27] or, if the CRC was previously heated on a different parent body, deposited from a fluid). The solubility[39] of Na_2SO_4 drops exponentially with temperature below 32 °C, suggesting that the majority of sulfate precipitation in the CRC occurred at temperatures comparable to or lower than those (~0 to 88 °C) inferred from isotopic studies for aqueous alteration of the CR parent body[40,41]. This may indicate that the sulfate formed near the end of the asteroid's hydrothermal processing phase after cooling from higher temperatures or that, locally, the CRC and surrounding matrix never reached temperatures as high as experienced elsewhere on

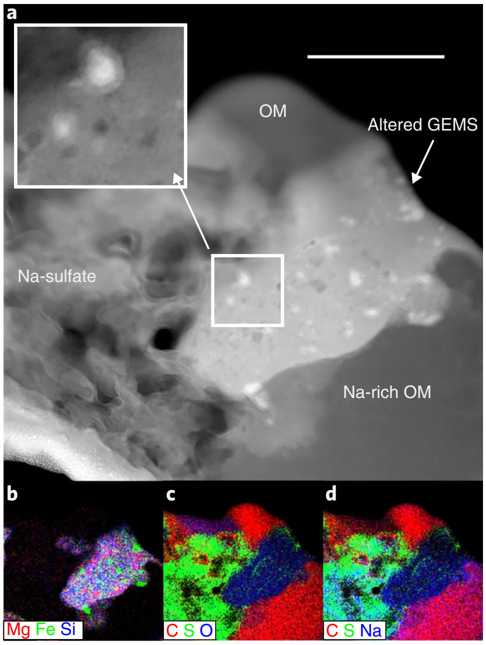

Fig. 7 | STEM data for ^{16}O-poor CRC FIB section. a–d, STEM-HAADF (**a**) and EDS composite colour maps corresponding to indicated elements (**b–d**) of altered GEMS and Na-sulfate from near the top of the section with ^{16}O-rich material (Fig. 5b and Supplementary Fig. 7). The inset in **a** shows the presence of oxidation rims on the metal grains. Additional quantification of the EDS spectrum images is included in Supplementary Fig. 6 and Supplementary Table 6. Scale bar, 200 nm.

the parent asteroid. The concentration of ^{16}O-poor sulfates near the upper-left clast-matrix interface (Fig. 3) suggests that the sulfate-rich fluid concentrated there. We note that this side of the CRC is situated very near a chondrule (Fig. 1), which may have locally affected fluid flow. The high presolar grain abundance and the largely unaltered nature of many silicates and GEMS grains indicate that the aqueous alteration only minimally affected most of the inorganic components of the CRC, probably due to these materials being protected by the highly abundant OM and/or relatively low-temperature alteration. One UCAMM shows evidence, in the form of unusual GEMS compositions, for a very limited degree of aqueous alteration[27], but sulfates were not reported. The lack of similar sulfates in UCAMMs to those seen in the CRC likely indicates either that their parent bodies never experienced the aqueous alteration conditions needed to produce them or that they were dissolved during isolation of the micrometeorites from Antarctic snow and/or ice.

The CRC likely originated from the materials available in the outer disk region where Kuiper Belt objects formed and represents a primordial building block of C-rich icy bodies. Formation of the CRC via cosmic-ray processing of the surface of an icy body, as proposed for some UCAMMs[10,42], is highly unlikely due to the long irradiation time required, tens of million years, compared with the few million years timescale of chondrite formation. The lower D/H of the CRC's OM, compared with OM in CR chondrites and the most extreme UCAMMs and IDPs, may represent a temporal change in the composition of refractory OM in the outer Solar System: presolar or early-formed material was more D-rich, while material that formed more slowly, for example, via ultraviolet processing of organic precursors[43], was less anomalous. If such a temporal evolution in cometary D/H exists, it would not be surprising for cometary materials sampled by CR chondrites to be less anomalous, since these meteorites have the youngest accretion ages[44]. Analysis of Stardust mission comet Wild 2 samples revealed efficient outward radial transport of materials to the comet-forming region of the protoplanetary disk[45]. The presence of the CRC in LAP 02342 indicates that inward transport also affected the late stages of planetesimal accretion, and provides further support for a connection between comets and C-asteroids[1,46,47], with the latter largely accreting from similarly primitive materials, but containing less C and ice. Moreover, as suggested for the CRC, the possibility that cometary microxenoliths in primitive chondrites retain isotopic and/or chemical signatures of their original ices provides a novel way to study the properties of the most primitive ice-rich materials from the early Solar System. Future dedicated searches for additional ultracarbonaceous microxenoliths in the most primitive carbonaceous chondrites may prove valuable for expanding our understanding of the full range of primitive astromaterials in the early Solar System.

Methods

Optical and scanning electron microscopy. We investigated a thin section of LAP 02342 provided by NASA's Johnson Space Center. Following optical mapping at the Institute of Space Sciences (CSIC-IEEC) by a Zeiss Scope petrographic microscope, detailed backscattered electron imaging and elemental X-ray analyses were performed with two field emission scanning electron microscopes: an FEI Quanta 650 at CSIC-IEEC and a JEOL 6500F at the Carnegie Institution, both equipped with Oxford silicon drift X-ray detectors. Selected areas (Fig. 1 and Supplementary Fig. 1) were then targeted for analysis with a Cameca NanoSIMS 50L ion microprobe at the Carnegie Institution. Areas were analysed by SEM both before and after the SIMS measurements.

NanoSIMS measurements. NanoSIMS measurements were carried out in automated imaging mode with a focused (~100 nm) Cs$^+$ primary ion beam and simultaneous collection of negative secondary ions. A total of approximately 30,000 µm^2 were mapped for C and O isotopes together with ^{28}Si and ^{27}Al^{16}O to search for presolar grains, 7,000 µm^2 to characterize H, C and N isotopes and an additional 8,000 µm^2 for just D/H ratios and elemental C. Methods were very similar to those described by Nittler et al.[15].

The L'image software (L. R. Nittler) was use to analyse the SIMS image data. Images were corrected for the 44 ns deadtime of the electron multiplier counting system and for shifts between frames (via an autocorrelation algorithm). The O isotopic images were also corrected for quasi-simultaneous arrival effects, which can lead to undercounting of ^{16}O and introduce an isotopic fractionation[48]. See Nittler et al.[15] for more details.

Following the deadtime, alignment and quasi-simultaneous arrival corrections, we calculated pixel-by-pixel isotopic ratio images (that is, ^{17}O/^{16}O, ^{18}O/^{16}O, ^{13}C/^{12}C, ^{15}N/^{14}N, D/H). O isotopic ratios were internally standardized to the average values measured in each 12 × 12 µm image. A synthetic powder with composition $C_{30}H_{50}O$ and purified insoluble organic matter from CR2 chondrite QUE 99177[3] were used as isotopic standards for the H, N and C data.

Presolar O-rich (for example, silicate and oxide) and C-rich (that is, SiC) grain candidates were identified by manual examination of each isotopic ratio images and the corresponding 'sigma' images, in which each pixel represents the number of standard deviations (based on Poisson statistics) its measured isotopic ratio is away from terrestrial values. Candidate grain regions of interest (ROIs) were selected as multiple adjacent pixels that clearly deviate from the standard ratio(s). Isotopic ratios were subsequently calculated from the summed counts of all pixels within an ROI. An ROI was considered to be anomalous if at least one isotopic ratio was more than 3σ away from the isotopic ratio of surrounding meteorite matrix. To characterize organic materials, we used an automatic particle definition algorithm[49] to define individual C-rich ROIs in the images and calculated C, N and H isotopic ratios from the summed pixel counts. Diameters of presolar grains were estimated from the full width at half maximum of the anomalous regions and corrected for a 120 nm beam broadening as described in ref. [15].

Since the NanoSIMS primary ion beam tails contribute some signal from surrounding material to the measurement of grains of interest, all reported isotopic anomalies are considered to be lower limits. In particular, measured D/H ratios are lower limits due to the possibility of terrestrial contamination on the sample surface.

Presolar grain abundance estimates. To quantify the concentrations of presolar grains in the different imaged regions, we divided the total area covered by the grains by the total imaged area for each region, excluding cracks and other void space. The total area of the CRC imaged for O isotopes was 4,000 µm^2, of the matrix was approximately 12,800 µm^2 and of the S-rich rim was approximately 9,900 µm^2. Based on thresholding the NanoSIMS O and C images, we estimated that silicate material makes up 33% of the imaged portion of the CRC. Therefore, the presolar silicate abundance reported in the main text for the CRC was based on an imaged area of 1,300 µm^2. The lower limit on the presolar abundance given in the text was estimated by assuming that the total CRC area imaged is the sum of the 1,300 μm^2 O-rich portion and half the C-rich area (1,300 μm^2) to correct for the lower density of the organic matter, assumed to be two times lower than that of the silicate material. Errors in presolar grain abundances were derived by using a recently described Monte Carlo method that accounts for uncertainty in grain diameter determination[15]. Note that for consistency, comparison data in Fig. 2b only include datasets measured under similar conditions to the present study. Recent higher-spatial-resolution studies[50] have indicated that presolar silicates are at least a factor of two higher in the most primitive meteorites (for example, Acfer 094).

FIB sample preparation. We extracted a total of seven cross-sections (Supplementary Fig. 7) by means of FIB lift-out methods: two matrix sections; three clast sections; and one section transecting an ^{16}O-poor region identified near the edge of the clast. All sections were prepared with a FEI Nova 600 FIB-SEM at the US Naval Research Laboratory, using a 30 keV Ga$^+$ ion beam. Progressively lower ion beam currents were used as the sections were thinned to reduce the amorphous damage layer on the front and back surfaces. Thinning of sections below approximately 1 μm was carried out without SEM observation to preserve carbon functional chemistry in the sample[51].

Scanning transmission X-ray microscopy. X-ray absorption imaging and XANES measurements were performed at the 5.3.2.2 beamline at the Advanced Light Source, Lawrence Berkeley National Laboratory, Berkeley, CA. Carbon, N and Fe photoabsorption edges were targeted to gain information on organic functional chemistry and the oxidation state of organic and inorganic components of the FIB lift-out sections. XANES spectra are derived from X-ray absorption one-dimensional or two-dimensional images by calculating the ratio of photoabsorption (I) by a ROI with that of the background (I_0), as $-\ln(I/I_0)$. No significant polarization effects were observed, owing to the extremely fine-grained nature of the components in each FIB section and the randomized orientations of these components. Generation of XANES spectra from scanning transmission X-ray microscopy data, XANES spectral deconvolution and calibration of the intensity ratio curves was automated in Python.

We note that the C-XANES data from the edge section in Fig. 4, but not the other sections, were acquired after STEM analysis, raising the possibility of modification of the functional chemistry in the sample due to beam damage by the 60 keV electrons. However, we did not find evidence for such damage, as it would be expected to decrease the apparent carboxyl abundance, whereas the opposite trend is observed.

Scanning transmission electron microscopy. STEM studies of five of the sections were performed with the Nion UltraSTEM200-X at the US Naval Research Laboratory. The UltraSTEM was operated at 60 kV, with a nominal probe size of 150 pm and probe currents of 50–150 pA. Bright-field and dark-field STEM images were recorded as 1,024 × 1,024 pixel images. Image mosaics shown in Fig. 5 and Supplementary Fig. 3 were created from individual 1 μm field of view images.

The 0.7 sr, windowless Bruker energy dispersive X-ray spectrometer was used for elemental mapping. The maps were acquired as full spectrum images at 512 × 512 pixels, and processed with Cliff–Lorimer routines using k-factors calculated to conform to the individual detector performance, with the Bruker Espirit 2.0 software. The bremsstrahlung background subtraction and detector energy gain calibration were individually verified for each quantified spectrum. Additional quantification details are provided in the Supplementary information.

Data availability

The data that support the plots within this paper and other findings of this study are available from the corresponding author upon reasonable request.

Received: 12 July 2018; Accepted: 26 February 2019;

References

1. Kruijer, T. S., Burkhardt, C., Budde, G. & Kleine, T. Age of Jupiter inferred from the distinct genetics and formation times of meteorites. *Proc. Natl Acad. Sci. USA* **114**, 6712–6716 (2017).
2. Weisberg, M. K., Prinz, M., Clayton, R. N. & Mayeda, T. K. The CR (Renazzo-type) carbonaceous chondrite group and its implications. *Geochim. Cosmochim. Acta* **57**, 1567–1586 (1993).
3. Alexander, C. M.O'D., Fogel, M., Yabuta, H. & Cody, G. D. The origin and evolution of chondrites recorded in the elemental and isotopic compositions of their macromolecular organic matter. *Geochim. Cosmochim. Acta* **71**, 4380–4403 (2007).
4. Nguyen, A. N., Nittler, L. R., Stadermann, F. J., Stroud, R. M. & Alexander, C. M. O'D. Coordinated analyses of presolar grains in the Allan Hills 77307 and Queen Elizabeth Range 99177 meteorites. *Astrophys. J* **719**, 166–189 (2010).
5. Van Kooten, E. M. M. E. et al. Isotopic evidence for primordial molecular cloud material in metal-rich carbonaceous chondrites. *Proc. Natl Acad. Sci. USA* **113**, 2011–2016 (2016).
6. Howard, K. T., Alexander, C. M. O'D., Schrader, D. L. & Dyl, K. A. Classification of hydrous meteorites (CR, CM and C2 ungrouped) by phyllosilicate fraction: PSD-XRD modal mineralogy and planetesimal environments. *Geochim. Cosmochim. Acta* **149**, 206–222 (2015).
7. Schramm, L. S., Brownlee, D. E. & Wheelock, M. M. Major element composition of stratospheric micrometeorites. *Meteoritics* **24**, 99–112 (1989).
8. Thomas, K. L., Blanford, G. E., Keller, L. P., Klock, W. & McKay, D. S. Carbon abundance and silicate mineralogy of anhydrous interplanetary dust particles. *Geochim. Cosmochim. Acta* **57**, 1551–1566 (1993).
9. Duprat, J. et al. Extreme deuterium excesses in ultracarbonaceous micrometeorites from central Antarctic snow. *Science* **328**, 742–745 (2010).
10. Dartois, E. et al. UltraCarbonaceous Antarctic micrometeorites, probing the Solar System beyond the nitrogen snow-line. *Icarus* **224**, 243–252 (2013).
11. Dartois, E. et al. Dome C ultracarbonaceous Antarctic micrometeorites: infrared and Raman fingerprints. *Astron. Astrophys.* **609**, A65 (2018).
12. Trigo-Rodríguez, J. M. et al. Evidence for extended aqueous alteration in CR carbonaceous chondrites. *Lunar Planet. Sci.* **44**, abstr. 1929 (2013).
13. Wasson, J. T. & Rubin, A. E. Composition of matrix in the CR chondrite LAP 02342. *Geochim. Cosmochim. Acta* **73**, 1436–1460 (2009).
14. Trigo-Rodriguez, J. M. & Blum, J. Tensile strength as an indicator of the degree of primitiveness of undifferentiated bodies. *Planet. Space Sci.* **57**, 243–249 (2009).
15. Nittler, L. R. et al. High abundances of presolar grains and ^{15}N-rich organic matter in CO3.0 chondrite dominion range 08006. *Geochim. Cosmochim. Acta* **226**, 107–131 (2018).
16. Floss, C. & Haenecour, P. Presolar silicate grains: abundances, isotopic and elemental compositions, and the effects of secondary processing. *Geochem. J.* **50**, 3–25 (2016).
17. Davidson, J. et al. Abundances of presolar silicon carbide grains in primitive meteorites determined by NanoSIMS. *Geochim. Cosmochim. Acta* **139**, 248–266 (2014).
18. Sakamoto, N. et al. Remnants of the early Solar System water enriched in heavy oxygen isotopes. *Science* **317**, 231–233 (2007).
19. Starkey, N. A., Franchi, I. A. & Lee, M. R. Isotopic diversity in interplanetary dust particles and preservation of extreme ^{16}O-depletion. *Geochim. Cosmochim. Acta* **142**, 115–131 (2014).
20. Busemann, H. et al. Interstellar chemistry recorded in organic matter from primitive meteorites. *Science* **312**, 727–730 (2006).
21. Urquhart, S. G. & Ade, H. Trends in the carbonyl core (C 1s, O 1s) $\rightarrow \pi^*_{C=O}$ transition in the near-edge X-ray absorption fine structure spectra of organic molecules. *J. Phys. Chem. B* **106**, 8531–8538 (2002).
22. Alexander, C. M. O'D., Cody, G. D., Gregorio, B. T. D., Nittler, L. R. & Stroud, R. M. The nature, origin and modification of insoluble organic matter in chondrites, the major source of Earth's C and N. *Chem. Erde* **77**, 227–256 (2017).
23. Keller, L. P. & Messenger, S. On the origins of GEMS grains. *Geochim. Cosmochim. Acta* **75**, 5336–5365 (2011).
24. Le Guillou, C., Changela, H. G. & Brearley, A. J. Widespread oxidized and hydrated amorphous silicates in CR chondrites matrices: implications for alteration conditions and H_2 degassing of asteroids. *Earth Planet. Sci. Lett.* **420**, 162–173 (2015).
25. Abreu, N. M. Why is it so difficult to classify Renazzo-type (CR) carbonaceous chondrites? Implications from TEM observations of matrices for the sequences of aqueous alteration. *Geochim. Cosmochim. Acta* **194**, 91–122 (2016).
26. Bradley, J. P. et al. An infrared spectral match between GEMS and interstellar grains. *Science* **285**, 1716–1718 (1999).
27. Yabuta, H. et al. Formation of an ultracarbonaceous Antarctic micrometeorite through minimal aqueous alteration in a small porous icy body. *Geochim. Cosmochim. Acta* **214**, 172–190 (2017).
28. Nakamura-Messenger, K., Clemett, S. J., Messenger, S. & Keller, L. P. Experimental aqueous alteration of cometary dust. *Meteorit. Planet. Sci.* **46**, 843–856 (2011).
29. Leroux, H., Cuvillier, P., Zanda, B. & Hewins, R. H. GEMS-like material in the matrix of the Paris meteorite and the early stages of alteration of CM chondrites. *Geochim. Cosmochim. Acta* **170**, 247–265 (2015).
30. Alexander, C. M. O'D. et al. The provenances of asteroids, and their contributions to the volatile inventories of the terrestrial planets. *Science* **337**, 721–723 (2012).
31. Matrajt, G., Messenger, S., Brownlee, D. & Joswiak, D. Diverse forms of primordial organic matter identified in interplanetary dust particles. *Meteorit. Planet. Sci.* **47**, 525–549 (2012).
32. Floss, C., Noguchi, T. & Yada, T. Hydrogen and nitrogen imaging of Ultra-Carbonaceous Antarctic Micrometeorite TT54B397. *Meteorit. Planet. Sci. Suppl.* **76**, 5230 (2013).
33. Trigo-Rodríguez, J. M. & Llorca, J. On the sodium overabundance in cometary meteoroids. *Adv. Space Res.* **39**, 517–525 (2007).
34. Trigo-Rodríguez, J. M., Llorca, J. & Fabregat, J. Chemical abundances determined from meteor spectra—II. Evidence for enlarged sodium abundances in meteoroids. *Mon. Not. R. Astron. Soc.* **348**, 802–810 (2004).
35. McKeegan, K. D. et al. The oxygen isotopic composition of the Sun inferred from captured solar wind. *Science* **332**, 1528–1532 (2011).

36. Lyons, J. R. & Young, E. D. CO self-shielding as the origin of oxygen isotope anomalies in the early solar nebula. *Nature* **435**, 317–320 (2005).
37. Yurimoto, H. & Kuramoto, K. Molecular cloud origin for the oxygen isotope heterogeneity in the Solar System. *Science* **305**, 1763–1766 (2004).
38. Labidi, J., Farquhar, J., Alexander, C. M. O'D., Eldridge, D. L. & Oduro, H. Mass independent sulfur isotope signatures in CMs: implications for sulfur chemistry in the early Solar System. *Geochim. Cosmochim. Acta* **196**, 326–350 (2017).
39. Bharmoria, P., Gehlot, P. S., Gupta, H. & Kumar, A. Temperature-dependent solubility transition of Na_2SO_4 in water and the effect of NaCl therein: solution structures and salt water dynamics. *J. Phys. Chem. B* **118**, 12734–12742 (2014).
40. Alexander, C. M. O'D., Bowden, R., Fogel, M. L. & Howard, K. T. Carbonate abundances and isotopic compositions in chondrites. *Meteorit. Planet. Sci.* **50**, 810–833 (2015).
41. Jilly-Rehak, C. E., Huss, G. R., Nagashima, K. & Schrader, D. L. Low-temperature aqueous alteration on the CR chondrite parent body: implications from in situ oxygen-isotope analyses. *Geochim. Cosmochim. Acta* **222**, 230–252 (2018).
42. Augé, B. et al. Irradiation of nitrogen-rich ices by swift heavy ions: clues for the formation of ultracarbonaceous micrometeorites. *Astron. Astrophys.* **592**, A99 (2016).
43. Ciesla, F. J. & Sandford, S. A. Organic synthesis via irradiation and warming of ice grains in the solar nebula. *Science* **336**, 452–454 (2012).
44. Sugiura, N. & Fujiya, W. Correlated accretion ages and ε^{54}Cr of meteorite parent bodies and the evolution of the solar nebula. *Meteorit. Planet. Sci.* **49**, 772–787 (2014).
45. Brownlee, D. et al. Comet 81P/Wild 2 under a microscope. *Science* **314**, 1711–1716 (2006).
46. Schrader, D. L. et al. The retention of dust in protoplanetary disks: evidence from agglomeratic olivine chondrules from the outer Solar System. *Geochim. Cosmochim. Acta* **223**, 405–421 (2018).
47. Briani, G., Morbidelli, A., Gounelle, M. & Nesvorný, D. Evidence for an asteroid–comet continuum from simulations of carbonaceous microxenolith dynamical evolution. *Meteorit. Planet. Sci.* **46**, 1863–1877 (2011).
48. Slodzian, G., Hillion, F., Stadermann, F. J. & Zinner, E. QSA influences on isotopic ratio measurements. *Appl. Surf. Sci.* **231–232**, 874–877 (2004).
49. Nittler, L. R., Alexander, C. M. O'D., Gao, X., Walker, R. M. & Zinner, E. Stellar sapphires: the properties and origins of presolar Al_2O_3 in meteorites. *Astrophys. J.* **483**, 475–495 (1997).
50. Hoppe, P., Leitner, J. & Kodolányi, J. The stardust abundance in the local interstellar cloud at the birth of the Solar System. *Nat. Astron.* **1**, 617–620 (2017).
51. Bassim, N. D. et al. Minimizing damage during FIB sample preparation of soft materials. *J. Microsc.* **245**, 288–301 (2012).

Acknowledgements

J.M.T.-R. and C.E.M.-C. acknowledge funding support from Spanish grants AYA 2011-26522 and AYA 2015-67175-P. C.E.M.-C. and S.T. participated in this study in the frame of a PhD in Physics at the Autonomous University of Barcelona. L.R.N., C.M.O'D.A., R.M.S. and B.T.D. acknowledge funding support from NASA grants NNX10AI63G and NNH16AC42I. This research used resources of the Advanced Light Source, which is a DOE Office of Science User Facility under contract no. DE-AC02-05CH11231. We thank H. Yabuta and J. Duprat for helpful comments that improved this paper.

Author contributions

J.M.T.-R. and C.E.M.-C. identified the C-rich clast and brought it to the attention of the other authors. J.M.T.-R., L.R.N. and R.M.S. designed the study. All authors participated in data acquisition and analysis. L.R.N. and J.M.T.-R. wrote the paper with substantial input from other authors.

Competing interests

The authors declare no competing interests.

Additional information

Supplementary information is available for this paper at https://doi.org/10.1038/s41550-019-0737-8.

Reprints and permissions information is available at www.nature.com/reprints.

Correspondence and requests for materials should be addressed to L.R.N.

Journal peer review information: *Nature Astronomy* thanks Jean Duprat, Hikaru Yabuta and the other anonymous reviewers for their contribution to the peer review of this work.

nature astronomy

SUPPLEMENTARY INFORMATION

https://doi.org/10.1038/s41550-019-0737-8

In the format provided by the authors and unedited.

A cometary building block in a primitive asteroidal meteorite

Larry R. Nittler[1]*, Rhonda M. Stroud[2], Josep M. Trigo-Rodríguez[3,4], Bradley T. De Gregorio[2], Conel M. O'D. Alexander[1], Jemma Davidson[1,5], Carles E. Moyano-Cambero[3,4] and Safoura Tanbakouei[3,4]

[1]Department of Terrestrial Magnetism, Carnegie Institution of Washington, Washington, DC, USA. [2]Materials Science and Technology Division, Code 6366, US Naval Research Laboratory, Washington, DC, USA. [3]Meteorites, Minor Bodies and Planetary Sciences Group, Institute of Space Sciences (CSIC), Barcelona, Catalonia, Spain. [4]Institut d'Estudis Espacials de Catalunya (IEEC), Barcelona, Catalonia, Spain. [5]Center for Meteorite Studies, School of Earth and Space Exploration, Arizona State University, Tempe, AZ, USA. *e-mail: lnittler@ciw.edu

A cometary building block in a primitive asteroidal meteorite

Larry R. Nittler[1], Rhonda M. Stroud[2], Josep M. Trigo-Rodríguez[3,4], Bradley T. De Gregorio[2], Conel M. O'D. Alexander[1], Jemma Davidson[1,5], Carles E. Moyano-Cambero[3,4], and Safoura Tanbakouei[3,4]

[1]Department of Terrestrial Magnetism, Carnegie Institution of Washington, Washington DC 20015, USA.

[2]U.S. Naval Research Laboratory Code 6366, 4555 Overlook Ave. SW, Washington DC 20375, USA.

[3]Institute of Space Sciences (CSIC), Meteorites, Minor Bodies and Planetary Sciences Group, Campus UAB Bellaterra, c/Can Magrans s/n, 08193 Cerdanyola del Vallès (Barcelona), Catalonia, Spain.

[4]Institut d'Estudis Espacials de Catalunya (IEEC), c/Gran Capità 2-4, Edifici Nexus, Despatx 201, 08034 Barcelona, Catalonia, Spain.

[5]Center for Meteorite Studies, School of Earth and Space Exploration, Arizona State University, 781 East Terrace Road, Tempe, AZ 85287, USA.

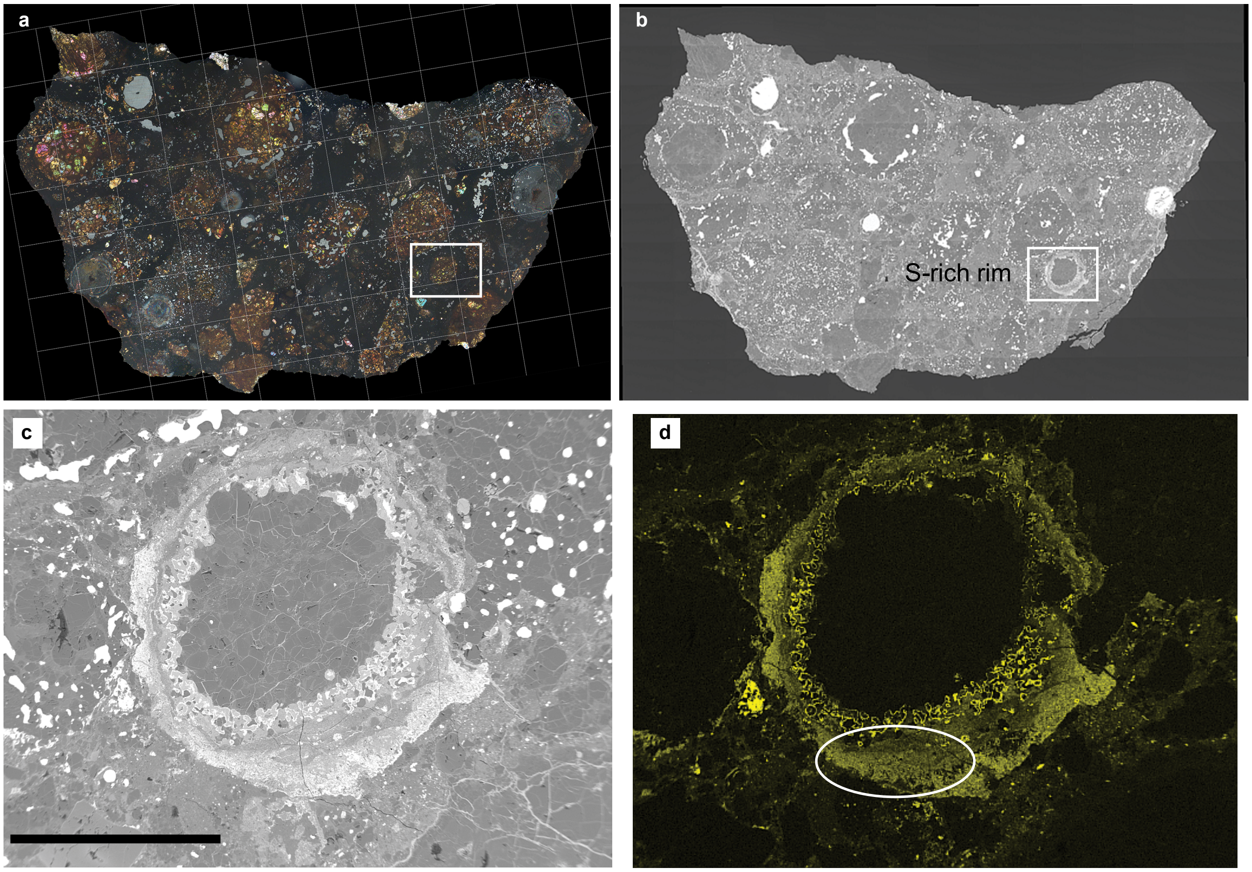

Supplementary Figure 1. S-rich chondrule rim (SRR) in LAP 02342 targeted for NanoSIMS measurements. The polished thin section is shown in **a** transmitted polarized light and **b** secondary electrons; the box indicates location of panels c and d. **c** SEM micrograph and **d** EDS-based S-map of the SRR. Ellipse indicates region analyzed by NanoSIMS. The scale bar in c is 500 μm.

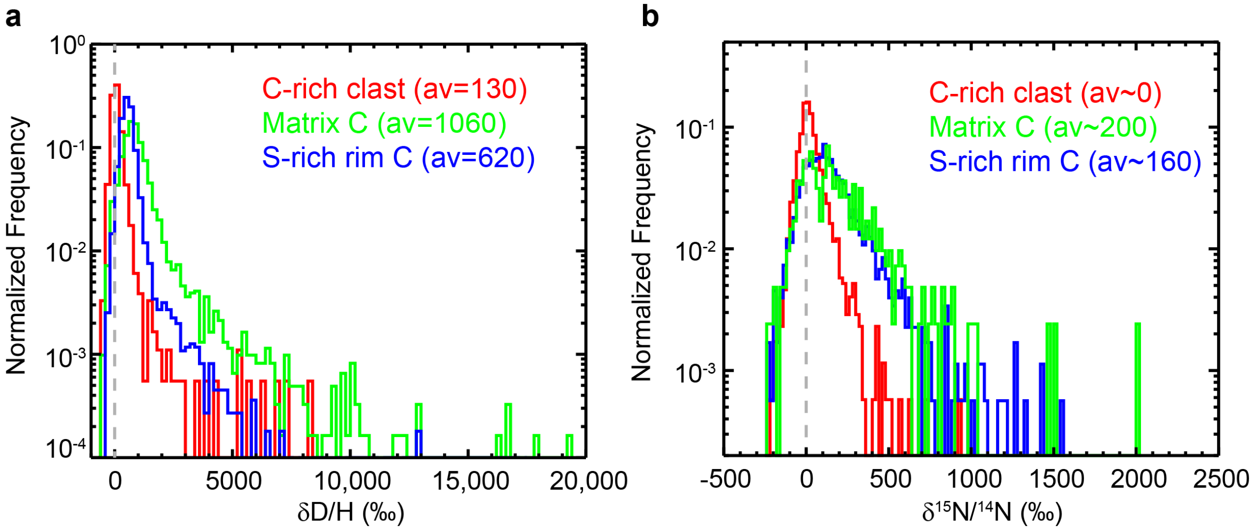

Supplementary Figure 2. Histograms of **a** δD/H and **b** $\delta^{15}N/^{14}N$ values in individual carbonaceous ROIs defined in NanoSIMS images from three analyzed lithologies (C-rich clast, matrix and S-rich rim; Figs. 1, S1). The C-rich clast is clearly less anomalous on average than other LAP 02342 materials, but still contains "hotspots" of anomalous materials (cf. Fig. 4).

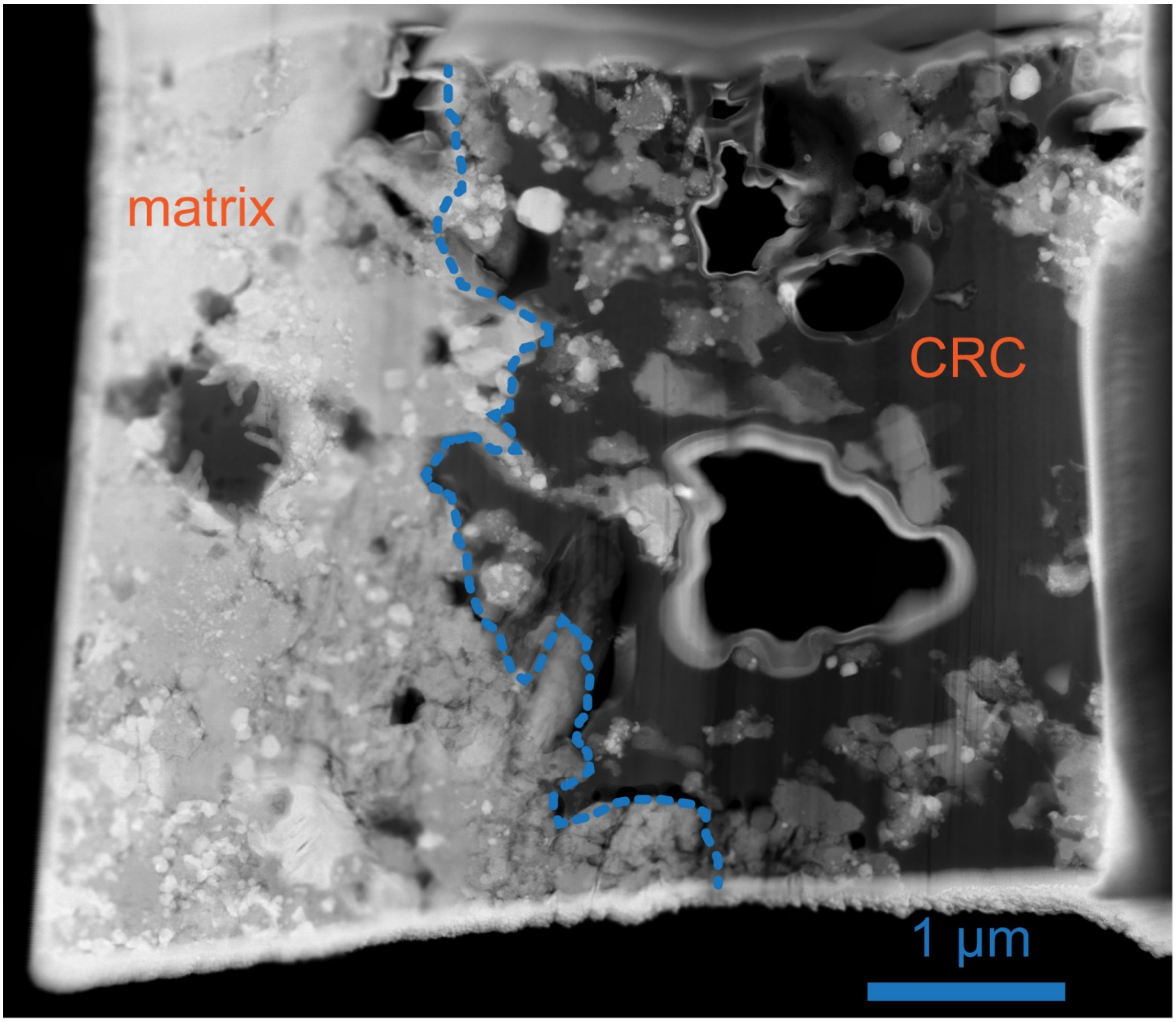

Supplementary Figure 3. HAADF STEM image mosaic of a FIB section (section e in Supplementary Fig. 7) crossing the edge of the CRC. The clear dichotomy between the CRC (right side) and surrounding LAP 02342 matrix (left side) is visible. The CRC side is dominated by organic matter (dark grey) and pore space (black), whereas the matrix is dominated by silicates (medium grey), metal and sulfides (white / light grey).

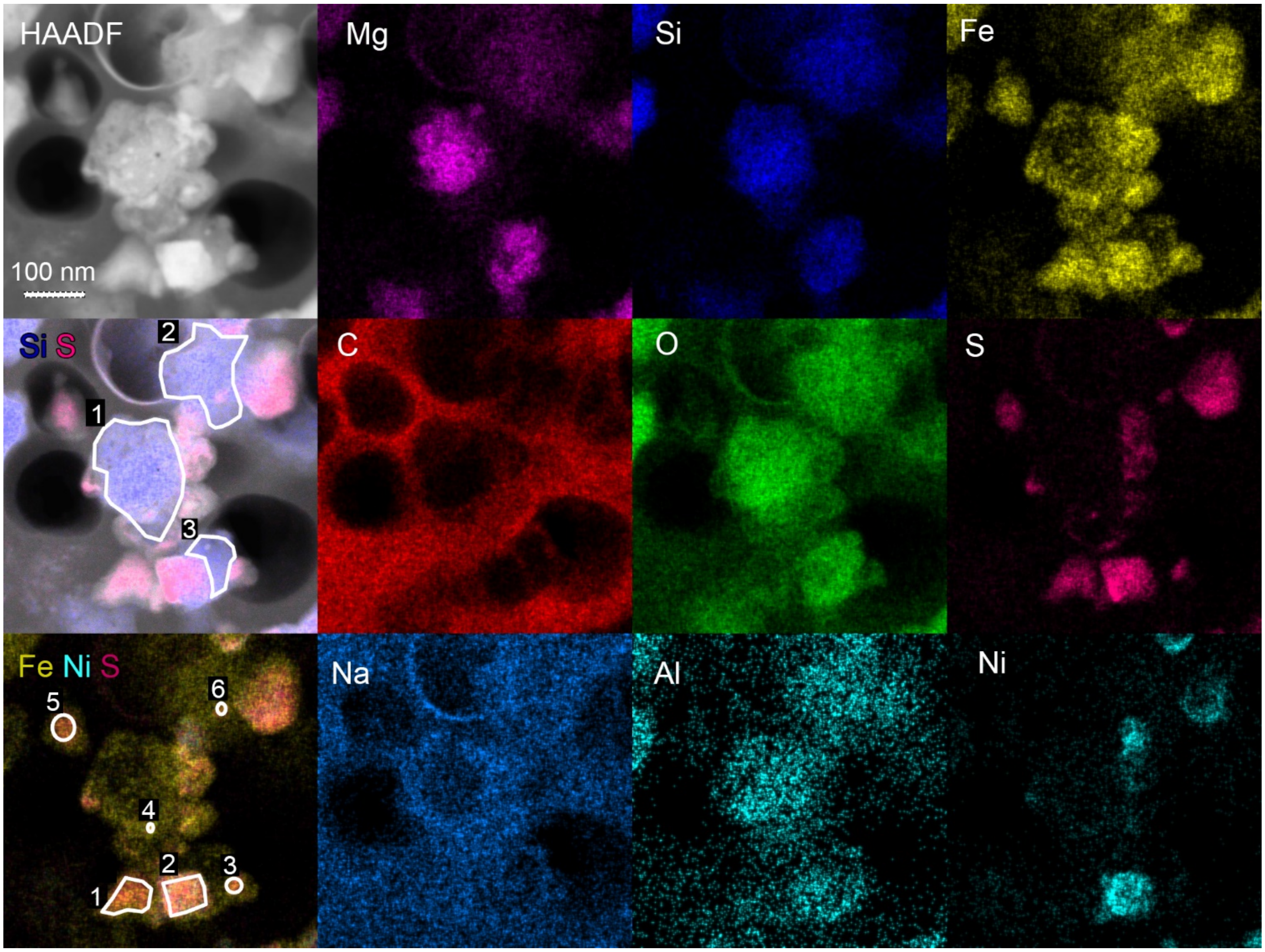

Supplementary Figure 4. STEM-EDS spectrum image of GEMS, sulfides and organic matter in the ^{16}O-poor section of the clast. The elemental maps are shown as raw counts with 3 pixel averaging, extracted from the full 512 px × 512 px spectrum image. Areas for sum spectrum quantification of GEMS (see Table S3), and sulfides (see Table S4) are indicated in the Si-S overlay map, and in the Fe-Ni-S overlay map respectively. The quantification boundaries for the GEMS quantification are drawn based on objects in the Si map modified to avoid large external sulfides, while including small internal metal and sulfide grains. The Fe and S elemental maps confirm that the high-Z grains visible inside the central GEMS in HAADF image are metal and sulfide grains. The Na appears to be associated with C and O on the surface of the central GEMS grain, and not incorporated into the interior.

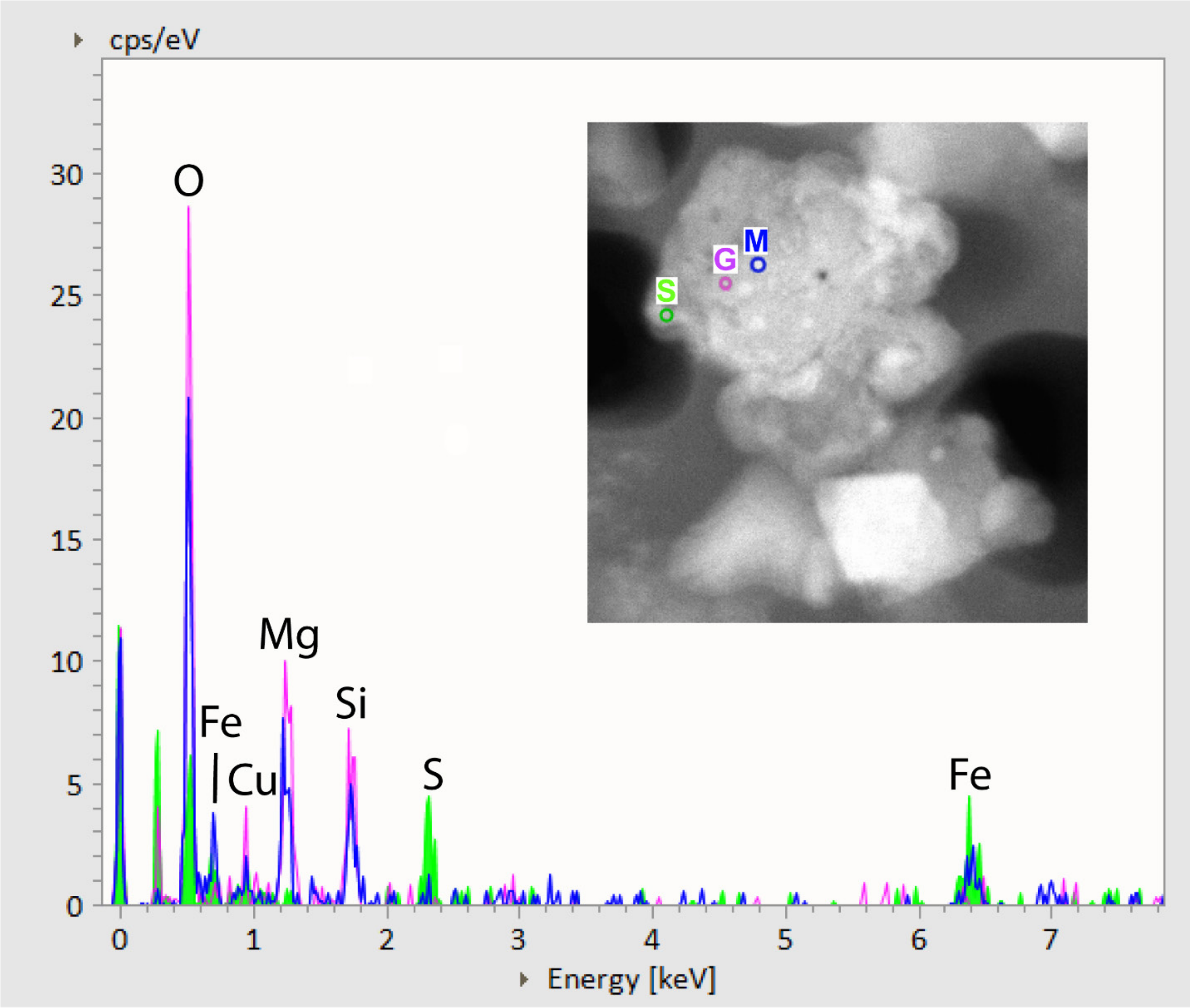

Supplementary Figure 5. STEM-EDS spectra extracted from full the spectrum image in metal (M), glass (G) and sulfide (S) regions in a GEMS grain. The extracted spectra are normalized to the counts in the zero-energy peak which scales with area. Some contribution from the glass is present in the metal spectrum due to the size (~ 8 nm) of the metal grain, which is much less than the thickness of the section. The quantification of these spectra is shown in Supplementary Table 5.

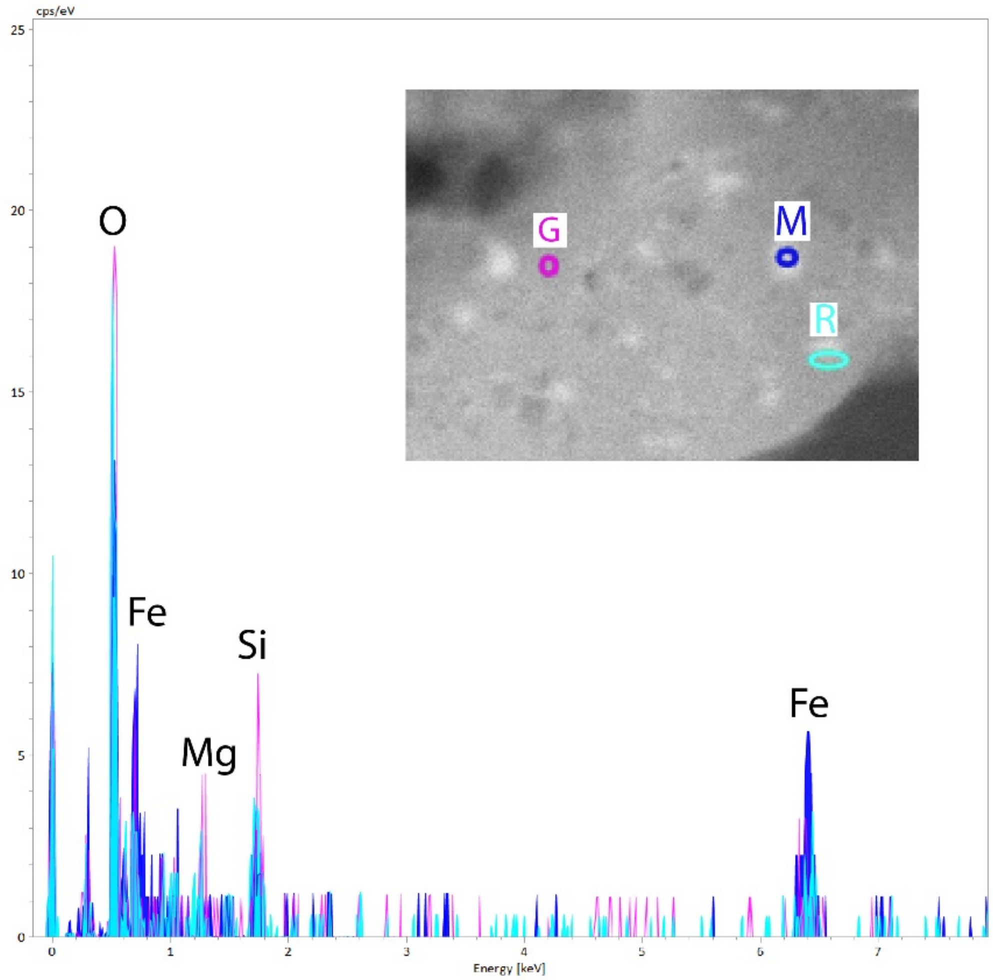

Supplementary Figure 6. STEM-EDS Spectra of glass (G), the core of a rimmed metal grain (M), and oxidized rim (R) of a metal grain in the altered GEMS (shown in Fig.7). The spectra are normalized to the Fe K edge intensity for direct comparison of the relative oxygen contents. The oxidized rim and metal core regions are thinner than the FIB section total, and thus show some contributions from underlying glass, however the rim spectrum clearly shows much greater oxidation. The quantification of these spectra is shown in Supplementary Table 6.

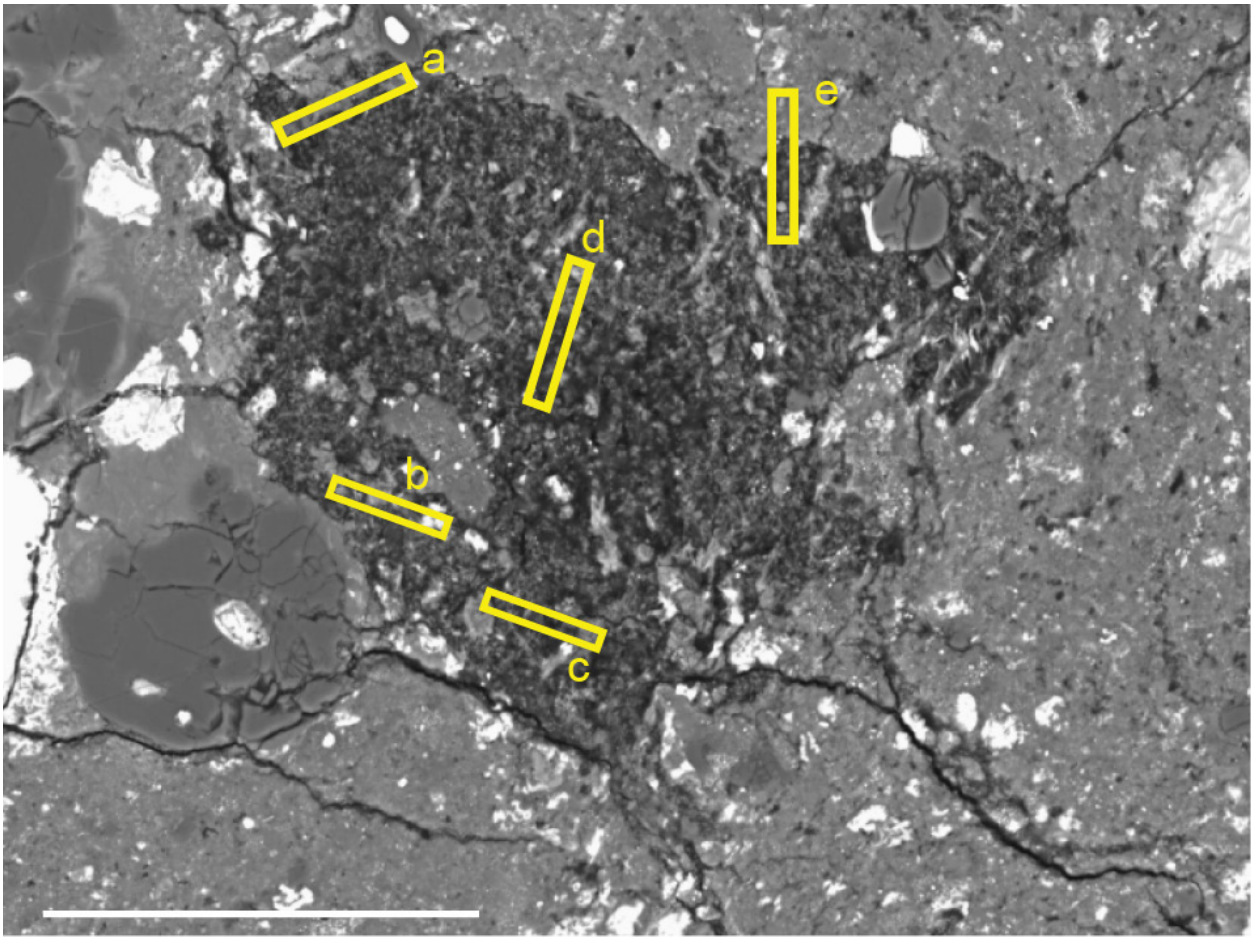

Supplementary Figure 7. Locations of FIB sections from CRC in LAP 02342. Section a transects ^{16}O-poor material and was analyzed by both TEM and STXM (Figs 4d, 5-7). Sections b and c were analyzed by TEM and d and e by STXM (Figs. 4d, Supplementary Fig. 6). The scale bar is 50 µm.

Supplementary Table 1. Presolar silicate grains in LAP 02342

Grain	Lithology[a]	Diameter[b] (nm)	$^{17}O/^{16}O$ ($\times10^{-4}$)	$^{18}O/^{16}O$ ($\times10^{-3}$)	Si^-/O^-	AlO^-/O^-
LAP-1	CRC	385	5.22 ± 0.16	1.717 ± 0.031	0.020	0.0062
LAP-2	CRC	279	4.41 ± 0.25	2.338 ± 0.057	0.015	0.0024
LAP-3	CRC	377	6.42 ± 0.22	2.022 ± 0.039	0.019	0.0027
LAP-4	CRC	354	7.18 ± 0.23	2.091 ± 0.038	0.023	0.0066
LAP-5	CRC	303	5.52 ± 0.21	2.048 ± 0.039	0.017	0.0063
LAP-6	Matrix	174	5.47 ± 0.39	2.028 ± 0.073	0.010	0.0006
LAP-7	Matrix	236	8.43 ± 0.54	1.400 ± 0.081	0.007	0.0061
LAP-8	Matrix	204	5.72 ± 0.40	1.594 ± 0.073	0.027	0.0014
LAP-9	Matrix	211	6.61 ± 0.49	2.101 ± 0.085	0.018	0.0008
LAP-10	Matrix	290	5.82 ± 0.36	1.628 ± 0.065	0.020	0.0009
LAP-11	CRC-mx	294	6.10 ± 0.23	1.917 ± 0.042	0.019	0.0030
LAP-12	CRC-mx	317	4.84 ± 0.20	1.989 ± 0.039	0.018	0.0054
LAP-13	CRC-mx	236	18.04 ± 0.57	1.961 ± 0.060	0.025	0.0025
LAP-14	SRR	253	9.36 ± 0.28	1.948 ± 0.041	0.010	0.0025
LAP-15	SRR	362	6.03 ± 0.20	1.642 ± 0.036	0.018	0.0035
LAP-16	SRR	258	5.13 ± 0.24	1.991 ± 0.047	0.014	0.0051
LAP-17	SRR	247	7.09 ± 0.32	1.795 ± 0.053	0.014	0.0040
LAP-18	SRR	204	7.83 ± 0.58	1.893 ± 0.091	0.020	0.0015

[a] CRC=C-rich clast, SRR=S-rich chondrule rim

[b] Estimated from NanoSIMS images and corrected for beam broadening

Supplementary Table 2. Oxygen isotopes of ^{16}O-poor ROIs in LAP 02342 C-rich clast (Fig. 3 of main text)*

ROI	δ^{17}O/^{16}O (±1σ)	δ^{18}O/^{16}O (±1σ)	Diameter (μm)
ROI 1	89 ± 17	135 ± 7	1.04
ROI 2	187 ± 32	174 ± 14	0.65
ROI 3	114 ± 36	172 ± 16	0.56
ROI 4	109 ± 34	158 ± 15	0.53
ROI 5	159 ± 38	147 ± 16	0.50
ROI 6	226 ± 35	158 ± 15	0.59
ROI 7	163 ± 37	157 ± 16	0.55
ROI 8	148 ± 39	158 ± 17	0.53
ROI 9	106 ± 29	130 ± 13	0.58
ROI 10	104 ± 32	141 ± 14	0.55
ROI 11	136 ± 28	128 ± 12	0.61
ROI 12	187 ± 58	202 ± 25	0.37
ROI 13	135 ± 41	146 ± 18	0.48
ROI 14	100 ± 33	131 ± 15	0.53
ROI 15	153 ± 47	174 ± 21	0.47
ROI 16	123 ± 29	148 ± 13	0.70
ROI 17	144 ± 36	147 ± 16	0.59
ROI 18	135 ± 37	123 ± 16	0.51
ROI 19	125 ± 33	135 ± 14	0.61
ROI 20	94 ± 27	116 ± 12	0.63
ROI 21	178 ± 38	149 ± 16	0.58
ROI 22	122 ± 35	123 ± 15	0.54
ROI 23	128 ± 42	112 ± 18	0.38
ROI 24	117 ± 33	116 ± 14	0.57
ROI 25	241 ± 52	145 ± 22	0.48
ROI 26	171 ± 40	126 ± 17	0.47
ROI 27	102 ± 30	115 ± 13	0.58
ROI 28	128 ± 34	118 ± 15	0.50
ROI 29	119 ± 31	123 ± 14	0.56
ROI 30	132 ± 42	126 ± 18	0.44
ROI 31	107 ± 35	123 ± 15	0.54
ROI 32	101 ± 27	91 ± 12	0.58
ROI 33	120 ± 33	118 ± 14	0.60
ROI 34	210 ± 51	118 ± 21	0.44
ROI 35	145 ± 35	93 ± 15	0.46
ROI 36	91 ± 30	99 ± 13	0.60
ROI 37	155 ± 40	109 ± 17	0.51
ROI 38	156 ± 47	122 ± 20	0.45
ROI 39	164 ± 50	138 ± 21	0.54
ROI 40	170 ± 47	145 ± 20	0.52
ROI 41	129 ± 37	95 ± 16	0.48

*Only grains with >3σ anomalies in ^{17}O and >5σ anomalies in ^{18}O are included. Mean values (± $2\sigma_{mean}$) are: δ^{17}O=140 ±11, δ^{18}O=134±7; these values are displayed as an error ellipse in Figure 3 of main text.

Supplementary Table 3. Compositions (atomic ratios) of GEMS grains identified in LAP 02342 C-rich clast compared to those in interplanetary dust particles

	O/Si	Mg/Si	Al/Si	S/Si	Cl/Si	Ca/Si	Fe/Si	Ni/Si
^{16}O-poor								
GEMS 1	6.487	1.182	0.095	0.089	0.017	0.018	0.556	0.019
GEMS 2	6.123	1.423	0.036	0.054	0.012	0.01	0.308	0.006
GEMS 3	6.052	0.622	0.101	0.086	0.019	0.007	0.632	0.012
Altered GEMS	7.107	0.585	0.093	0.077	0.01	0.017	0.747	0.024
Clast interior								
GEMS 1	4.96	0.782	0.117	0.175	0.023	0.001	1.091	0.079
GEMS 2	5.326	0.475	0.149	0.129	0.017	0.005	1.61	0.107
GEMS 3	5.74	0.516	0.158	0.124	0.018	0.013	1.407	0.079
Solar[a]	15.7	1.03	0.085	0.421	0.005	0.06	0.848	0.049
IDP GEMS[b]	2.4-4.6	0.05-1.44	0-0.21	0.01-1.25		0-0.23	0.96-1.63	0-0.12
IDP GEMS[c]	4.4	0.65	0.11	0.26		0.057	0.44	0.028
IDP GEMS[d]	3.27	0.73	0.07	0.31		0.04	0.56	0.03

[a] Lodders, K. Solar system abundances and condensation temperatures of the elements. *Ap. J.* **591**, 1220–1247 (2003).

[b] Keller, L. P. & Messenger, S. On the origins of GEMS grains. *Geochim. Cosmochim. Acta* **75**, 5336–5365 (2011).

[c] Ishii, H. A. *et al.* Comparison of Comet 81P/Wild 2 Dust with Interplanetary Dust from Comets. *Science* **319**, 447–450, doi:10.1126/science.1150683 (2008).

[d] Messenger, S., Nakamura-Messenger, K., Keller, L. P. & Clemett, S. J. Pristine stratospheric collection of interplanetary dust on an oil-free polyurethane foam substrate. *Meteorit. Planet. Sci.* **50**, 1468-1485 (2015).

Supplementary Table 4. Compositions of individual sulfide grains identified in Supplementary Fig. 4.

1					
Element	Net Counts	Mass [%]	Atom [%]	abs. error [%] (1 sigma)	rel. error [%] (1 sigma)
Carbon	2397				
Oxygen	2489				
Sodium	408				
Magnesium	121				
Aluminum	39				
Silicon	98				
Sulfur	1903	33.85	47.15	1.32	3.89
Iron	2441	65.01	51.99	2.43	3.74
Nickel	33	1.13	0.86	0.23	19.89

2					
Element	Net Counts	Mass [%]	Atom [%]	abs. error [%] (1 sigma)	rel. error [%] (1 sigma)
Carbon	290				
Oxygen	5048				
Sodium	198				
Magnesium	1647				
Aluminum	147				
Silicon	1327				
Sulfur	3562	36.49	50.37	1.29	3.53
Iron	2931	44.94	35.62	1.64	3.65
Nickel	1072	18.57	14.00	0.85	4.57

3					
Element	Net Counts	Mass [%]	Atom [%]	abs. error [%] (1 sigma)	rel. error [%] (1 sigma)
Carbon	148				
Oxygen	457				
Sodium	37				
Magnesium	38				
Aluminum	14				
Silicon	107				
Sulfur	312	33.14	46.37	2.20	6.64
Iron	406	64.64	51.93	3.96	6.13
Nickel	11	2.22	1.70	0.70	31.71

4

Element	Net Counts	Mass [%]	Atom [%]	abs. error [%] (1 sigma)	rel. error [%] (1 sigma)
Carbon	43				
Oxygen	170				
Sodium	12				
Magnesium	16				
Aluminum	5				
Silicon	38				
Sulfur	46	22.00	32.96	3.43	15.60
Iron	108	76.87	66.12	8.28	10.77
Nickel	1	1.12	0.92	1.04	93.12

5

Element	Net Counts	Mass [%]	Atom [%]	abs. error [%] (1 sigma)	rel. error [%] (1 sigma)
Carbon	254				
Oxygen	411				
Sodium	82				
Magnesium	4				
Aluminum	2				
Silicon	7				
Sulfur	675	35.43	48.88	1.79	5.05
Iron	814	63.97	50.67	3.10	4.84
Nickel	6	0.60	0.45	0.27	45.57

6

Element	Net Counts	Mass [%]	Atom [%]	abs. error [%] (1 sigma)	rel. error [%] (1 sigma)
Carbon	62				
Oxygen	356				
Sodium	30				
Magnesium	79				
Aluminum	17				
Silicon	101				
Sulfur	96	27.12	39.33	2.99	11.03
Iron	173	72.88	60.67	6.35	8.71
Nickel	0	0.00	0.00	0.00	0.00

Supplementary Table 5. Compositions of GEMS components identified in Supplementary Fig. 5.

Glass

Element	Net Counts	Mass [%]	Atom [%]	abs. error [%] (1 sigma)	rel. error [%] (1 sigma)	
Oxygen	114	47	59	10	21	
Magnesium	50	28	23	4	15	
Silicon	42	25	18	4	16	

Metal[a]

Element	Net Counts	Mass [%]	Atom [%]	abs. error [%] (1 sigma)	rel. error [%] (1 sigma)	
Silicon	56	21	17	3	14	
Magnesium	60	21	20	3	13	
Iron	37	21	9	4	18	
Oxygen	153	37	54	7	19	

Sulfide

Element	Net Counts	Mass [%]	Atom [%]	abs. error [%] (1 sigma)	rel. error [%] (1 sigma)	
Carbon	36					deconvoluted only
Oxygen	36					deconvoluted only
Sulfur	38	38	52	6	17	
Iron	41	62	48	10	17	

[a] The metal measurement samples metal and glass, because the metal grain is smaller than the sample thickness. To obtain the true glass composition, the glass fraction must be subtracted off. The glass has a (Mg+Si)/O ratio of 41/59 = 0.69, equal to the 37/54 of metal region. Thus the Fe is Fe^0 to within the uncertainty of the statistics. The nickel content of the metal was below detection limits.

Supplementary Table 6. Elemental compositions of altered GEMS components identified in Supplementary Fig. 6.

Glass

Element	Net Counts	Mass [%]	Atom [%]	abs. error [%] (1 sigma)	rel. error [%] (1 sigma)
Silicon	42	28	24	4	16
Magnesium	16	10	10	3	26
Iron	23	24	10	5	23
Oxygen	99	38	57	12	30

Metal [a]

Element	Net Counts	Mass [%]	Atom [%]	abs. error [%] (1 sigma)	rel. error [%] (1 sigma)
Silicon	14	11	15	3	27
Iron	67	77	55	10	13
Oxygen	53	12	30	3	27

Oxidized Rim[b]

Element	Net Counts	Mass [%]	Atom [%]	abs. error [%] (1 sigma)	rel. error [%] (1 sigma)
Silicon	48	25	22	4	15
Magnesium	18	9	9	2	24
Iron	40	32	15	6	17
Oxygen	123	34	54	10	28

[a] The metal core measurement necessarily samples the oxidized rim and glassy matrix, due to the metal particle size relative to the sample thickness (~100 nm).

[b] The oxidized metal rim necessarily samples the rim and the glassy matrix, due to the size of the rim compared to the thickness of the section (~100 nm).

Supplementary Table 7. Energy Dispersive X-ray Counting Statisitcs for GEMs shown in Supplementary Fig 4.[a,b,c]

Element	Net Counts	Mass [%]	Atom [%]	abs. error [%] (1 σ)	rel. error [%] (1 σ)	Normalized to Si
GEMS 1						
Iron	8529	15.547	5.869	0.525	3.377	0.56
Sulfur	1180	1.437	0.945	0.086	5.984	0.09
Oxygen	40803	52.000	68.524	1.606	3.089	6.48
Aluminum	1150	1.379	1.077	0.083	6.033	0.10
Silicon	11880	14.078	10.568	0.157	1.117	1.00
Magnesium	12996	14.486	12.566	0.478	3.299	1.19
Nickel	332	0.683	0.245	0.070	10.262	0.02
Calcium	278	0.392	0.206	0.053	13.444	0.02
Copper	14114					
Carbon	7308					
Gallium	165					
Platinum	241					
Sodium	3308					
Chlorine	159					
GEMS 2						
Iron	6405	18.633	7.099	0.637	3.418	0.62
Sulfur	892	1.734	1.150	0.104	6.017	0.10
Oxygen	26258	53.409	71.029	1.661	3.110	6.19
Aluminum	823	1.576	1.243	0.098	6.202	0.11
Silicon	8011	15.150	11.478	0.198	1.309	1.00
Magnesium	4966	8.834	7.734	0.318	3.603	0.67
Nickel	155	0.510	0.185	0.071	14.003	0.02
Calcium	61	0.155	0.082	0.045	29.272	0.01
Copper	9787					
Carbon	4139					
Gallium	488					
Platinum	212					
Sodium	2427					
Chlorine	160					
GEMS 3						
Iron	1069	11.272	4.121	0.525	4.66	0.39
Sulfur	135	0.950	0.605	0.114	12.01	0.06
Oxygen	7288	53.750	68.588	1.756	3.27	6.49
Aluminum	125	0.869	0.657	0.107	12.36	0.06
Silicon	2179	14.942	10.862	0.353	2.36	1.00

Magnesium	2772	17.879	15.019	0.660	3.69	1.38	
Nickel	11	0.149	0.052	0.070	47.12		bdl
Calcium	20	0.189	0.096	0.067	35.54		bdl
Copper	2031						
Carbon	1049						
Gallium	40						
Platinum	46						
Sodium	328						
Chlorine	24						

[a] elements with only net counts reported are due either to artifacts (Ga and Pt from FIB preparation, Cu from the sample support) or surrounding materials (C, Na, Cl)

[b] elements with counting statistics leading to 1 σ errors > 30% are listed are below detection limit (bdl).

[C] Reported numbers for O are upper limits, due to contributions from underlying organic matter.